Nanotechnology **18** (2007) 195305 (11pp) doi:10.1088/0957-4484/18/19/195305

Focused ion beam scan routine, dwell time and dose optimizations for submicrometre period planar photonic crystal components and stamps in silicon

Wico C L Hopman[1], Feridun Ay[1], Wenbin Hu[1,3], Vishwas J Gadgil[1], Laurens Kuipers[2], Markus Pollnau[1] and René M de Ridder[1]

[1] MESA+Institute for Nanotechnology, University of Twente, PO Box 217, 7500 AE Enschede, The Netherlands
[2] FOM Institute for Atomic and Molecular Physics (AMOLF), Kruislaan 407, 1098 SJ Amsterdam, The Netherlands

E-mail: W.C.L.Hopman@utwente.nl and R.M.deRidder@utwente.nl

Received 13 February 2007, in final form 21 March 2007
Published 17 April 2007
Online at stacks.iop.org/Nano/18/195305

Abstract
Focused ion beam (FIB) milling is receiving increasing attention for nanostructuring in silicon (Si). These structures can for example be used for photonic crystal structures in a silicon-on-insulator (SOI) configuration or for moulds which can have various applications in combination with imprint technologies. However, FIB fabrication of submicrometre holes having perfectly vertical sidewalls is still challenging due to the redeposition effect in Si. In this study we show how the scan routine of the ion beam can be used as a sidewall optimization parameter. The experiments have been performed in Si and SOI. Furthermore, we show that sidewall angles as small as 1.5° are possible in Si membranes using a spiral scan method. We investigate the effect of the dose, loop number and dwell time on the sidewall angle, interhole milling and total milling depth by studying the milling of single and multiple holes into a crystal. We show that the sidewall angles can be as small as 5° in (bulk) Si and SOI when applying a larger dose. Finally, we found that a relatively large dwell time of 1 ms and a small loop number is favourable for obtaining vertical sidewalls. By comparing the results with those obtained by others, we conclude that the number of loops at a fixed dose per hole is the parameter that determines the sidewall angle and not the dwell time by itself.

(Some figures in this article are in colour only in the electronic version)

1. Introduction

The ultimate goal of integrated optics is to achieve full control of light propagation. Functional devices based on classical planar optical waveguiding in low to moderate refractive index contrast systems are reaching the limits of achievable complexity due to the necessarily large bend radii [1]. One possible route towards increasing integration density by several orders of magnitude is using so-called 'photonic crystal slabs' (PCSs), which have recently received much attention. By introducing 'defects' in a PCS in a controlled manner, one is able to implement passive and active building blocks (e.g. filters [2], sensors [3], and lasers [4]). Important breakthroughs have been reported on nano-cavities having Q-factors [5] exceeding 10^5 [6] and their applications as filters and even as all-optical transistors [7]. The reduction

[3] Present address: Fiber Optic Sensing R&D Center, Wuhan University of Technology, 430070, Wuhan, People's Republic of China.

 © 2007 IOP Publishing Ltd Printed in the UK

of the group velocity in PCS structures by several orders of magnitude [8] and their application as a tuneable time delay has also been reported [9]. A typical PCS structure consists of a high-refractive-index layer (e.g. Si, GaAs) perforated with a 2D periodic lattice of air holes having a diameter of approximately half the lattice period. The layer is stacked between two semi-infinite claddings that can be either patterned or homogeneous. There are two coexisting confinement mechanisms of light in PCS: in-plane confinement by the photonic bandgap effect [10] and vertical confinement by refractive-index-guiding realized by an index contrast between the PCS and its claddings. The basic functional PCS-based building blocks (resonators, waveguides, filters, switches, etc) are relatively small structures (10–40 μm), which can be combined to form more complex large-scale architectures. Desired milling depths for photonic operation and moulds are between 100 and 200 nm [11] and the typical hole size is about 200–300 nm in diameter, arranged in a lattice with a periodicity around 0.5 μm [5, 7, 8, 12–14].

Focused ion beam (FIB) milling can be used to define these PCS structures in, for example, silicon, which can be used as a mould for nano-imprint lithography, or in a silicon on insulator (SOI) layer configuration suitable for photonic applications [14]. An important challenge for nanophotonics is its interfacing to the outside world. For guided-wave applications, it is often necessary to use relatively large-sized access waveguides that are usually defined using conventional lithography and etching methods. On the other hand, we have the small photonic crystal elements with features requiring sub-10 nm resolution, which should be accurately aligned with respect to the larger structures. Due to its inherent imaging and high-accuracy alignment properties, FIB is a promising tool for fabricating nanophotonic structures on substrates containing predefined microscopic and macroscopic waveguiding structures.

In opto-electronics, FIB has been applied for fabrication of micro-optical components with low surface roughness [15] and for defining the end facet mirrors for conventional semiconductor lasers [16]. It has also been applied for bulk micromachining of macro-porous silicon in order to fabricate 3D Yablonovite-like photonic crystals [17], and for fabricating 2D periodic, metal nanostructures [18] of which the shape of the primitive unit cell can be varied [19]. Another application of FIB has been the fabrication of quasi-2D photonic crystals by milling 1D gratings into freestanding multilayer membranes [20]. Direct FIB milling in silicon is still in an early state of maturity, the losses by modifications of the crystalline Si [21–23] induced by ion bombardment and implantation of, for example, gallium ions within the sample [24] are still too high [25] to realize high-quality PCS devices. However, some recent results have been achieved in lowering the losses by either using etch-assisting gasses [25, 26] or heat-treatments (out-diffusion of ions) [27, 28], which may lead to breakthroughs on this subject. The damaged Si at the Si–air interface may be removed by wet chemical etching [29]. On the other hand, FIB processing is an ideal candidate for fabrication of moulds, where the previously mentioned disadvantages of the ion milling process do not apply [11, 30, 31]. The smoothening effect of FIB processing [32] can, for example, be exploited for creating nanosmooth moulds and replicas.

Perfectly vertical sidewalls are, in principle, required for photonic applications to guarantee low-loss propagation; sidewall angles of 5° can already induce a 8 dB mm^{-1} propagation loss [33]. Fabricating submicron holes in silicon with perfectly vertical sidewalls by FIB milling is challenging due to the redeposition effect [23, 34–36]: sputtered Si atoms or clusters can be redeposited locally. This effect is less pronounced in the milling of slits (or trenches), which can result in sidewall angles up to a few degrees for low currents [37]. For similar structures as studied in this paper, sidewall angles of ∼9° have been reported obtained using a multi-pass type raster scan [38]. The redeposition effect becomes more dominant when the size of the holes is decreased. A straightforward solution for lowering the effects of redeposition by using a repetitive pass system was published in 1984 by Yamaguchi *et al* [39]. That work forms the basis for investigations on the milling properties that can be manipulated by varying the dwell time [40–42] (the time the beam is stationary at a fixed point), which may influence the number of repetition loops. However, dwell-times cannot be made arbitrarily small, because FIB does not provide infinite contrast between written and non-written areas. This is because a structure is defined using, for example, a raster scan while modulating the ion beam current. The ion beam cannot be completely turned off when moving sequentially from one pixel to the next, leading to unwanted milling of the nominally unwritten area. However, the contrast can be increased choosing an appropriate milling strategy, as we will show in this paper. Besides the contrast, the scan path of the ion beam can also influence the geometry of the milled structure. The most common scan routines are serpentine, raster, annulus and radial (or spiral), which are described in [35, 43]. The main method for analysing the geometry is cross-sectioning of the holes and subsequent inspection by scanning electron microscopy (SEM). The SEM photos are then further analysed to find the milling depths, sidewall angles and average hole diameters. The exact cross-sectioning method is presented first in detail in section 2.2, because we found that some cross-sectioning methods might influence the originally milled geometry leading to incorrect interpretations. In section 3, we compare the hole geometry obtained for two routines for bulk Si, SOI and Si membranes, namely raster and spiral scanning. The remainder of this paper refers to results obtained by using the spiral-scan routine. To optimize the sidewall angles of the submicrometre holes needed for photonic operation further, we investigated in section 4 the impact of a range of doses on the milling depth and sidewall angle for both individual holes and holes within a triangular-lattice crystal at 48 pA. Furthermore, in section 5 we present the dwell-time–loop-number-combination variation for a milling current of 48 pA, while keeping the total dose constant. Finally, the main conclusions are presented in section 6.

2. FIB processing

2.1. Machine properties and general settings

A dual-beam FIB machine, the Nova 600 from FEI Company, was used for processing our structures. This machine has the advantage that it contains both an ion beam and an e-beam

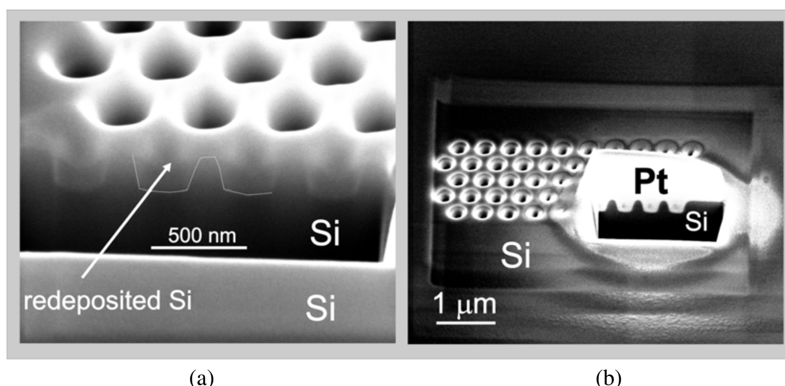

(a) (b)

Figure 1. Different methods for cross-sectioning. (a) Direct milling of a rectangular hole into the Si crystal; details can be found in the main text. (b) Cross-section milling after local metal (Pt) deposition.

column. This powerful combination allows for both charge-neutralization in the case of milling insulating materials, and non-destructive characterization by SEM. The ion beam is generated from a gallium liquid metal source. The field of view (FoV) of this FIB machine is divided into 4096 × 4096 pixels. The actual size of this grid depends on the magnification set prior to the milling. We used a magnification (in a view mode termed Quad-view) of 5000 (5 kX), resulting in a field of view of about 25 × 25 μm^2, and a minimum inter-pixel distance of 6.2 nm. For the experiments reported in this section the dwell time was predefined without optimizing at a value of 0.1 ms, which in our case resulted in a loop time of 6.0 s. All pixels are sequentially specified by their coordinates and dwell time. The $1/e$ ion beam spot-size was maintained at approximately 1.5 times the inter-pixel distance. This spot-size is mainly determined by the FIB milling current, which can be set in discrete steps by selecting an aperture size. Although the spot-size grows with the milling current, the lowest current (1.5 pA, spot-size = 7.5 nm) is not the optimum for practical reasons like the total milling-time and the feasible accuracy of focusing of the beam. In previous experiments we found that milling at 48 pA, which gives a spot-size of about 18 nm, provides for this FoV a good balance between milling time and accuracy. Switching between currents would be ideal for larger structures; the boundaries of the hole could then be defined at a low current (small spot-size). However, switching between currents and thus apertures is not an option in the FIB used in this research, because each aperture has a different focus and beam offset, which cannot (in our current machine) be programmed.

2.2. Cross-sectioning

In this work, cross-sections need to be realized in order to study how geometries of submicrometre-sized holes in several material systems are affected by the milling parameters. We tried several cross-sectioning techniques, namely milling of a hole with a sloped milling depth, line by line polishing, and combinations of these. In figure 1(a), a combination of both methods is used, first a big hole is milled at a current of 48 pA having a sloped bottom with the largest depth found at the cross-section interface; second a line by line milling strategy is applied at a lower current of 28 pA to achieve a smooth surface. The figure shows that redeposited material fills up the holes and possibly modifies the shape of the hole. One of the effects of redeposition is a very low contrast between the original un-milled Si and the milled holes. The shape may be partially resolved by using low acceleration voltages and a high resolution SEM machine to minimize the influence of the observed charging effect.

However, a better method, which is used for the Si and SOI milling experiments presented in this paper, is first locally depositing a layer of platinum (Pt) using the FIB and a precursor gas (methylcyclopentadienyl)trimethyl-platinum. Second, a hole is milled with a sloped bottom to avoid long milling times. Finally, a line by line scan (termed cleaning cross-section) is applied at a lower current (28 pA) to establish a high-contrast high-resolution image; see figure 1(b). Since the electron beam and the ion beam are arranged at a fixed angle of 52°, SEM photos at an angle can be made of the cross-section without rotating the stage. Small angles can be used for visualizing the cross-sections of deep holes to minimize the size and consequently the milling times of the large hole for cross-sectioning. Since the SEM photos are taken under an angle, the horizontal scale bar cannot be applied to the vertical direction. The length of the image in the vertical direction has to be scaled by $1/\sin$ (angle).

The membrane structures were cross-sectioned by milling a slit into the membrane using a current of 48 pA and fine-polishing using a line by line milling strategy at a current of 9.7 pA. Although redeposition on the sidewall cannot be completely avoided when using this procedure, we observed little difference when comparing the cross-sectioned membrane with the angled top view SEM images; an example is shown in figure 2.

3. Spiral scanning versus raster scanning

The standard scanning method used in most FIB applications is the raster scan, which is schematically shown in figure 3(a). The ion beam scans from one side to the other, while it mills for a specified dwell time at the pixel positions provided in the pattern definition file (here termed the stream file). Since the beam is not switched off between the holes, the scan routine causes interhole milling, which leads to the top surface in the entire FoV being lowered with respect to the surrounding

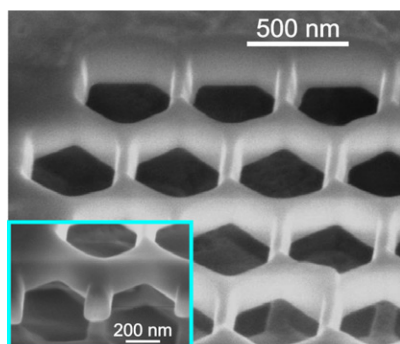

Figure 2. An example of a well defined FIB-milled planar PCS in a Si membrane (viewed at 52°). The hexagons shown here were rotated by 9° with respect to the photonic crystal lattice, in order to obtain an enlarged photonic bandgap [13]. Through the structure a 'shadow pattern' can be seen in the bottom silicon due to milling of the ion beam into the substrate. A cross-section (viewed at 35°) of the same structure made by milling a slit into the air-bridge PCS is shown in the inset. The structure was milled at 9.7 pA using a dwell time of 0.01 ms.

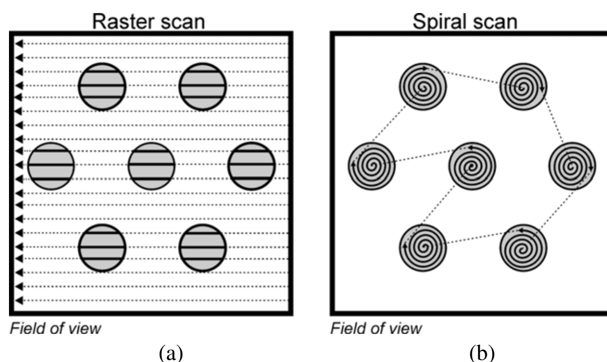

Figure 3. (a) Raster scanning. (b) Spiral scanning.

surface. We refer to this effect as the structure being 'sunk' into the substrate. A better method for milling arrays of holes is spiral scanning. A schematic drawing of the spiral scan is also shown in figure 3(b). The spiral scan significantly reduces the amount of interhole milling, as will be shown experimentally in the next section. This method is expected to produce more vertical sidewalls, because locally redeposited material is immediately milled away to a large extent. The method is tested on circular holes for reasons of obvious symmetry; however, the spiral scan method is also expected to yield results with respect to the decrease in interhole milling and the sidewall angle for non-circular holes. The spiral scan method may also be beneficial for holes having sharp corners; however, this has not been investigated in this research.

In section 3.1 we will compare the two scan routines, applied to 'bulk' Si for two doses. In section 3.2 the same experiment is repeated for SOI, and in section 3.3 the scan routines are evaluated on Si membranes.

3.1. Silicon

For the experiments reported here we mounted a piece of p-type Si ⟨100⟩ on a chuck using silver paint for providing a conducting path between the sample and the grounded holder. The electrical contact when using the paint is much better than for example is obtained using double-sided carbon tape. However, in some cases we noticed that the paint had a non-uniform layer thickness, resulting in specimens that were slightly tilted up to 2°, which may lead to asymmetrical holes. We designed two stream files defining 50 holes with 250 nm diameter and 440 nm periodicity. The raster scan file defined 64 689 pixels, whereas the spiral scan file comprised 59900 pixels. The difference, which is caused by the spiral pattern filling the circular hole shape more efficiently, leads to small differences in the dose per hole. The two writing patterns were compared for 12 and 36 repetitions (loops), resulting in milling depths of about 250 and 900 nm, respectively. The ratio between the number of loops and the milling depth is not linear due to the redeposition effect, as we will show in section 4. The spread in milling depth will both reveal the best method for fabricating holes suitable for photonic application (12 loops) and it can show the geometry differences when subjected to a high level of redeposition (36 loops).

Figure 4(a) shows the result of a 12-loop raster scan. The overview SEM and the cross-section were taken at an angle of 52°. Due to the angle, the scale bar in the vertical direction has to be multiplied by sin(52°) to match the scale bar displayed for the horizontal direction, as mentioned in section 2.2. Because the structure of holes is sunk into the host material, we define two milling depths, shown in the inset of figure 4(a). The first

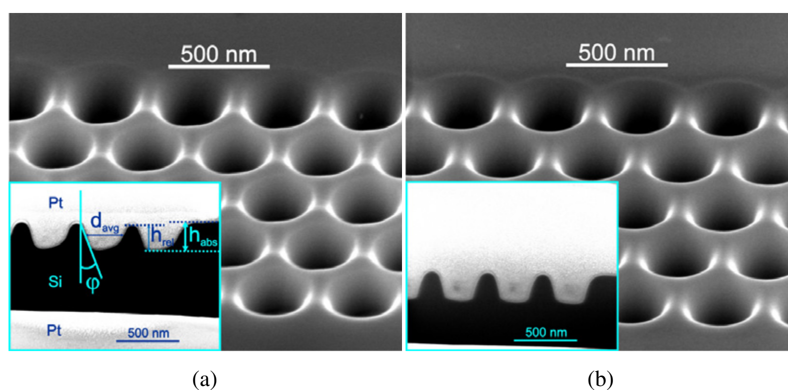

Figure 4. Patterns milled at 48 pA using 12 loops and 0.1 ms dwell time per pixel. All SEM images were taken at a 52° angle. The insets show the cross-sections. (a) Raster scan; (b) spiral scan.

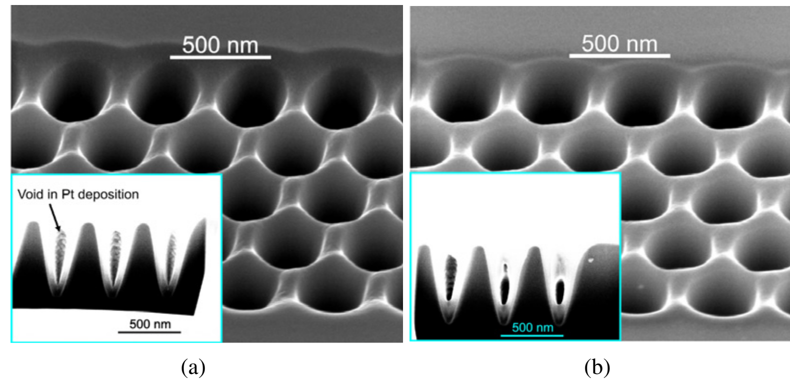

(a) (b)

Figure 5. Patterns milled at 48 pA in Si using 36 loops and 0.1 ms dwell time per pixel. The top view SEM images were taken at a 52° angle, and the cross-sections shown in the insets were taken at 45°. (a) Raster scan; (b) spiral scan.

Table 1. Comparison of raster and spiral milling in Si, SOI and Si membranes (Si-m).

Scan routine	Material	Pixels per hole	Loop-number	Dose/hole[a], D (pC)	Absolute depth, $h_{abs}\pm 3\%$ (nm)	Relative depth, $h_{rel}\pm 3\%$ (nm)	Average diameter, $d_{avg}\pm 5\%$ (nm)	Sidewall angle $\pm 10\%$ (deg)
Raster	Si	1293	12	75	253	214	299	19
Spiral	Si	1198	12	69	300	282	276	13
Raster	Si	1293	36	224	906	855	249	9
Spiral	Si	1198	36	207	917	885	232	8
Raster	SOI	1293	12	75	364	345	330	11
Spiral	SOI	1198	12	69	355	355	262	7
Raster	Si-m	1293	13	81	—	338	350	5
Spiral	Si-m	1198	13	75	—	339	380	5
Raster	Si-m	1293	20	115	—	470	366	<1.5

[a] The current and dwell times are fixed to 48 pA and 0.1 ms, respectively.

one is the total ('absolute') height h_{abs} from the bottom of the hole to the surface of the silicon (just outside the exposed area around the holes, which might be subject to swelling [44, 45]). The second one, the relative height h_{rel} is defined as the height difference between the bottom of the hole and the interhole sidewall. Furthermore, the average hole diameter is defined from the side view as the hole diameter at 0.5 h_{rel}. The sidewall angle φ is defined as the angle between the surface normal and the sloped sidewall, estimated around 0.5 h_{rel}. In some cases, for either scanning routine, the holes may show different angles at both sidewalls, which may be due to drift, sample-tilt or other mechanisms. Therefore, we took φ as the average angle of both visible sidewalls. Figure 4(b) shows the results of the spiral scan. Without detailed graphical analysis it can be seen that the spiral scan gives better defined features; the sidewall angles are much smaller. This can be explained from the scanning routines shown in figure 3; the raster scan passes over the Si sidewalls many more times than is the case for the spiral scan. Nevertheless, we always find rounding at the top and bottom of the hole, which cannot be avoided by maskless milling. A hard mask on top like Al_2O_3 [26] may reduce the rounding effect at the top. Another difference between the scan patterns that is apparent from figure 4 (see also figure 3), is the difference between h_{abs} and h_{rel} for both methods. Careful examination of the hole cross-sections reveals for the case of raster scanning a systematic difference between the sidewall angles measured on the right- and the left-hand side. A possible explanation will be given in section 3.2. The detailed analysis for comparison can be found in table 1.

Increasing the number of loops to 36 led to 'V' shaped holes. Figure 5 shows the results of both scan methods. Voids within the Pt are observed in the cross-section. The pattern obtained by the raster scan has sunk deeper into the Si host material, and when carefully examined the spiral scan results show a slightly better sidewall angle (8° versus 9°). Despite the 10% lower dose for the spiral scan, the milling depth is only 1% (11 nm) less. This may be partially explained by the non-linear relationship between dose and depth, which will be discussed in more detail in section 4. However, the difference may also be partly attributed to the difference in scanning method, indicating that the spiral scanning method is more efficient in sputtering the material out of the hole.

3.2. Silicon on insulator (SOI)

Photonic crystal slabs require that a core layer with a high refractive index, containing the periodic structure, is enclosed between two lower-index cladding layers, in order to confine the light by effective index guiding. Moreover, for obtaining a photonic bandgap the refractive index difference between core and cladding layers should be as large as possible. A high index contrast can be established using SOI (silicon on top of silicon dioxide) for infrared wavelengths, where Si forms the guiding layer. Since the Si top layer is stacked on top of an insulator, the milling performance may be quite different from that of bulk

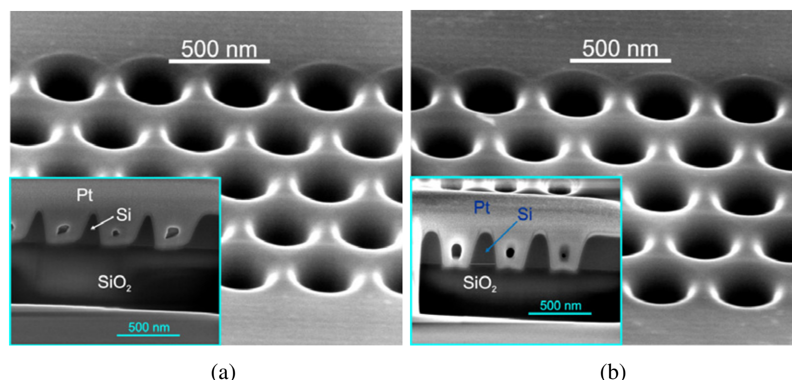

Figure 6. Hole arrays milled at 48 pA in SOI using 12 loops and 0.1 ms dwell time per pixel. The SEM images were taken at a 52° angle, leading to a vertical scaling factor of 1.27. (a) Raster scan; (b) spiral scan.

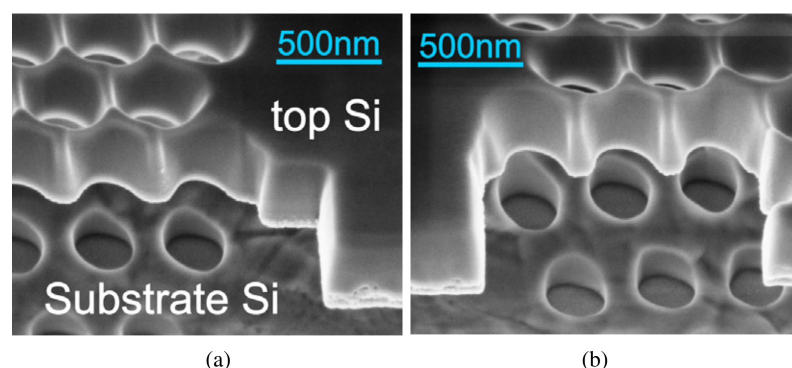

Figure 7. SOI membranes (the SiO_2 has been selectively removed) milled at 48 pA and 0.1 ms pixel dwell time. Both SEM pictures were taken at a 60° angle. The cross-section was made using a line by line milling method to reduce deposition. (a) Raster scan. (b) Spiral scan.

Si because the charge distributions are influenced. Applying a conductive metal layer first is not preferred, because the milling process may cause implantation of metal particles that will give rise to increased optical loss. Therefore, the FIB milling was performed on an unmodified SOI layer stack with a Si layer thickness of 340 nm and a buried oxide thickness of 1 μm.

The SOI milling results are depicted in figure 6. Although the angled top view SEM images suggest that the hole shape does not strongly depend on the choice of scanning scheme, the cross-sections reveal a considerable difference. Raster scanning gives thinner interhole sidewalls and the angles are on average worse than for spiral scanning. In section 3.1 it has already been observed that the raster method produces non-symmetrical shapes. This is a systematic effect originating from the scanning method, as can be seen in figures 4(a), 5(a) and 6(a). Because in the raster scan method the ion beam moves in vertical lines from right to left, the right part of the hole is milled earlier than the left part. Consequently the material milled from the left part may re-deposit on the right part, resulting in non-symmetric holes. The same explanation can be applied to the spiral method, which scans from the inside to the outside in concentric circles. As can be seen in figure 6(b), the inside of the hole is at lower depth than the outer part. Nevertheless, the hole is quite symmetric. This effect can be reduced by slightly decreasing the dwell time, i.e. using a higher number of passes. To do this without generating a larger amount of interhole milling, each hole has to be repeated several times in the stream file before jumping to the next hole. The major restriction for this method is the maximum allowed number of coordinates within the stream file, which is currently 10^6 for the used Nova 600 dual FIB. A further quantification of the geometries can be found in table 1.

3.3. Silicon membranes

Silicon membranes are important material hosts for photonic structures [9, 10], as they form a symmetric layer stack (air–Si–air) and maximize the index contrast (1–3.4–1@λ_0 = 1550 nm). Membrane-type PCSs, often termed air-bridge photonic crystals, are better suited for FIB milling than SOI-based PCSs because the redeposition effect is less severe in membranes. Two main factors contribute to this effect. First of all, the sputtered material can escape in two directions as soon as the bottom of the membrane has been reached. Second, by slightly overetching (milling) the holes, the redeposited material can be selectively removed, resulting typically in a ‘shadow pattern’ milled into the bottom substrate; see figures 2 and 7.

By comparing the realized hole diameters (350–380 nm) in figure 7 with the designed value (250 nm), we observed that holes milled through a membrane were larger than designed. This is caused by both the intentional over-milling and the more efficient milling process, due to the easier transport

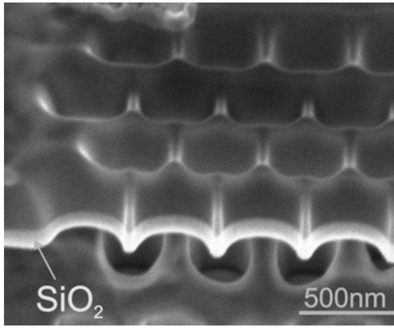

Figure 8. Milling result on a SOI membrane at 48 pA and 0.1 ms pixel dwell time. The pattern shows that with FIB a sidewall angle *of less than* 1.5° can be achieved. The SEM photograph is taken at a 30° angle.

of milled material from the forming hole. This increase of hole size can be easily compensated for in the design of the structure. From figure 7, we further find that both milling routines give similar average sidewall angles; see table 1. Increasing the over-milling time results in even better sidewall angles; see figure 8. We report a sidewall angle better than 1.5°, which can compete with the combination of direct e-beam lithography and reactive ion etching [46, 47].

4. Milling depth and sidewall angle versus dose in silicon

A linear relationship between the milling depth and dose can often be assumed for large d_{avg}/h_{abs} ratios. The local redeposition effect is not dominant in this regime, because the sputtered silicon can escape easily into the vacuum. The following relation has been found experimentally:

$$T = \frac{V}{IB}, \tag{1}$$

with I the milling current, T the milling time, V the sputtered volume and B the material-dependent sputter rate. The sputter rate for Si is 0.27 μm^3 nC^{-1} at 30 kV. To find the milling depth as a function of the dose, we can rewrite (1) using dose $D = IT$ and $V = 0.25\pi d_{avg}^2 h_{abs}$ as

$$h_{abs} = D\frac{4B}{\pi d_{avg}^2}. \tag{2}$$

The function shows a linear relation between the dose and the milling depth. However, in our case the ratio d_{avg}/h_{abs} is close to unity, making the redeposition more prominently observable. Therefore, the total volume that has to be milled is higher than the designed hole volume. Also, the sputter efficiency B can change because the ions impinge on a slanted surface (resulting in higher milling rates [48]), therefore (2) transforms into a nonlinear relation for small hole sizes. In this section, the milling depth and the sidewall angle is studied as a function of the applied dose. We distinguish two situations, a single milled hole and a hole within a crystal (an array of holes) to investigate the proximity effects.

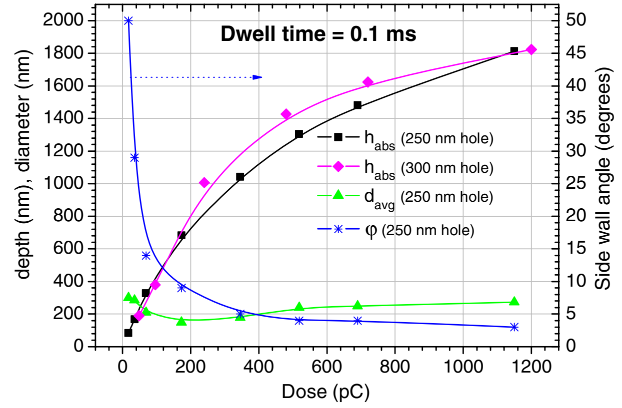

Figure 9. Milling results in bulk Si for a single hole as a function of dose. The designed hole diameter was 250 nm and the current and dwell time were fixed at 48 pA and 0.1 ms, respectively.

4.1. Single hole

In the 'single hole' experiment, the same 250 nm hole diameter was used as in the experiments mentioned in the previous sections. The hole was milled using the spiral scan strategy and the current and dwell time were fixed at 48 pA and 0.1 ms, respectively. The dose was varied by changing the loop number in discrete steps from three to 200, resulting in a dose variation between 17 and 1150 pC. The holes were cross-sectioned by the method described in section 2.2 and the SEM images were analysed to quantify the hole geometry.

The data obtained from the SEM images are shown in figure 9. The graphs shown in figure 9 can be used as calibration curves for milling individual 250 or 300 nm diameter holes. As expected, the figure shows that that the milling efficiency decreases with increasing milling depth. Moreover, we observe a strong decrease in sidewall angle at higher doses. In principle, this effect could be exploited for the fabrication of photonic components by designing the waveguiding layer to be at a depth where the sidewall angle and hole diameter have the desired values or using, for example, a sacrificial etch layer, but having the structures at the surface is for obvious reasons the most convenient choice. The observed large sidewall angles at low doses are caused by the rounding effect. Therefore, it is unlikely that the sidewall angle at the top can be lowered by increasing the dose. However, as previously mentioned, a hard mask could lower the rounding at the top of the hole. It can also be seen that the diameter defined at half the hole depth is approaching the designed value for higher doses. For comparison, we also milled a sequence of 300 nm diameter holes in Si using the FIB built-in spiral scan routine (not convenient for defining an array for holes) with the standard dwell time of 0.1 μs. Since the hole diameter is larger, the sputtered material can escape more easily, which results in higher milling depth for the dose range between 200 and 1000 pC. A collage of the SEM images can be found in figure 12. The data belonging to the curves in figure 9 can be found in table 3 for the 250 nm hole and in table 4 for the 300 nm hole.

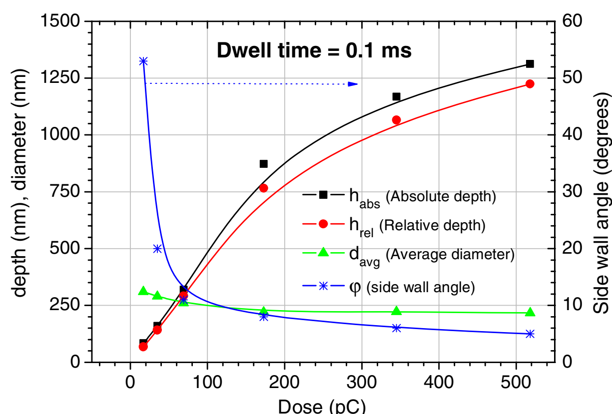

Figure 10. Milling results for holes in an array. The designed hole diameter was 250 nm and the current and dwell time were fixed to 0.1 ms and 48 pA, respectively.

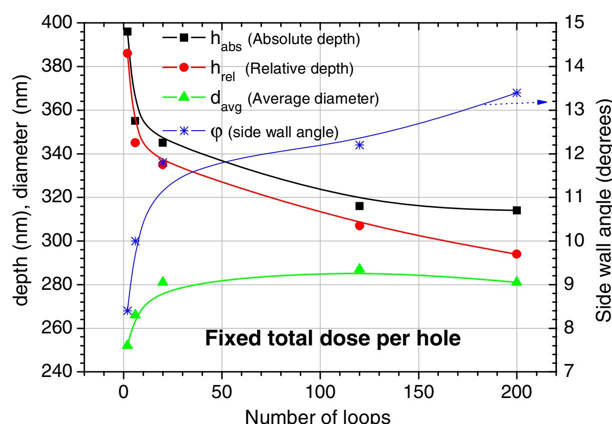

Figure 11. Milling results for a hole in an array, at a constant dose of 69 pC per hole. The designed hole diameter was 250 nm and the current was fixed at 48 pA.

4.2. Hole as an element of an array

In the previous section we showed the single hole milling results; however, for a PCS many holes arranged within, for example, a triangular or square lattice have to be milled. The geometry evolution at increasing dose is likely to differ from the single hole experiment due to proximity effects: milling of one hole interferes with the milling process of the surrounding holes in the array, resulting in different geometries. Another important effect for PCSs is the interhole milling, which manifests itself by the difference $h_{\mathrm{abs}} - h_{\mathrm{rel}}$. We studied the milling of holes in a triangular lattice having a 440 nm lattice constant. The dwell time was again fixed at 0.1 ms and the current at 48 pA.

In figure 10 we observe similar results for the milling of PCS holes as for single holes. However, an important difference is that in this case the milling depths are larger for the dose range studied here. As expected, the relative milling depth is smaller than the absolute milling depth. The figure suggests that the difference $h_{\mathrm{abs}} - h_{\mathrm{rel}}$ evolves to a constant value. The data can be found in table 5.

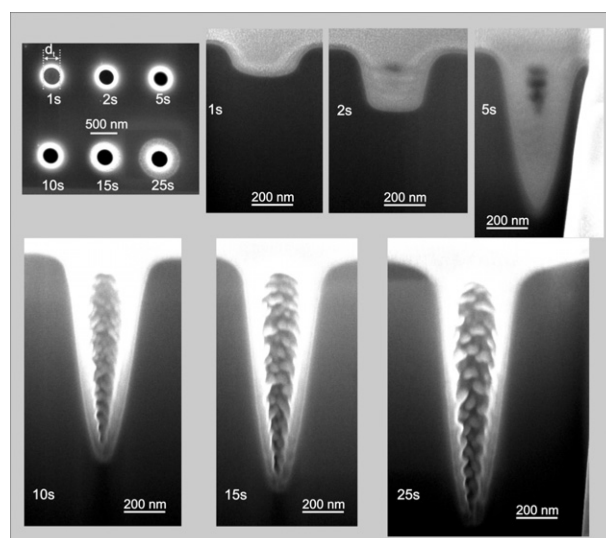

Figure 12. The effect of the dose on the geometry. The top left image shows a top view of all holes. The SEM images of the cross-sections in the top row are taken at a 52° angle, and the bottom row at 45°. The holes were designed using the FIB built-in procedure to an average diameter of 300 nm and the current and dwell time were fixed at 48 pA and 0.1 μs, respectively.

5. Dwell time and loop number variation

Besides optimizing the hole geometry by choosing an appropriate scan strategy, the geometry can also be favourably influenced by the dwell time [39, 41]. Varying the pixel dwell time implies a variation in dose, which makes the effect of the dwell time value less visible; see figures 9 and 10. Therefore, the dose was kept constant at 69 pC per hole while varying the combination loop number and dwell time. The loop number was varied from two to 200 and the dwell time from 6 μs to 0.6 ms.

The results of the experiments are displayed by the graphs in figure 11. They show that the most favourable conditions for milling are at low loop numbers and, consequently, at large dwell times around 1 ms for the studied dose. However in [41] it was reported that extremely large dwell times should be avoided. The figure also shows that the milling efficiency decreases for an increasing number of loops. Regarding the sidewall angle it is obviously not desired to have a high number of loops for a dose of 69 pC. A high loop number also increases the interhole milling drastically. These findings confirm the assumption that the dwell time is not the parameter that should be optimized but the dose per pixel per loop, or in other terms optimizing the number of loops while keeping the total dose per hole constant. In [49] it was suggested that smaller dwell times lead to better sidewall angles; however, the authors used a large current (>2.8 nA), which may explain their findings. The data from which the graphs in figure 11 have been constructed can be found in table 6.

Similar experiments were conducted on SOI for two currents; the results are shown in table 2. The values show a close resemblance to the values obtained from the Si milling experiment at 48 pA. Based on these results, we conclude that lowering the current does not lead to a significant reduction in sidewall angle at a dose around 60 pC. This seems to contradict

Table 2. Loop number variation of a hole within an array in SOI.

Current I (pA)	Loops	Dwell time (ms)	Dose per hole (pC)	Relative depth, $h_{rel} \pm 3\%$ (nm)	Average diameter, $d_{avg} \pm 5\%$ (nm)	Sidewall angle $\pm 5\%$ (deg)
48	2	1	61	286	282	7
9.7	6	1	59	320	258	7
9.7	62	0.1	66	349	255	11
9.7	617	0.01	66	301	210	20

Table 3. Values obtained from milling a single 250 nm diameter hole in Si.

Loops	Dose per hole[a], D (pC)	Absolute depth, $h_{abs} \pm 3\%$ (nm)	Average diameter, $d_{avg} \pm 5\%$ (nm)	Sidewall angle $\pm 10\%$ (deg)
3	17	84	300	50
6	35	169	285	29
12	69	328	210	14
30	173	683	150	9
60	345	1043	178	5
90	518	1305	240	4
120	690	1481	250	4
200	1150	1814	273	3

[a] Milled at 48 pA using a 0.1 ms dwell time.

Table 4. Values obtained from milling a single 300 nm diameter hole in Si.

Milling time, T (s)	Dose/ hole[a], D (pC)	Absolute depth, $h_{abs} \pm 3\%$ (nm)	Average diameter, $d_{avg} \pm 5\%$ (nm)	Sidewall angle $\varphi \pm 10\%$ (deg)
1	48	191	349	27
2	96	380	322	9
5	240	1007	280	8
10	480	1428	283	6
15	720	1624	305	5
25	1200	1823	291	4

[a] Milled at 48 pA using a 0.1 μs dwell time.

the observation published in [48], where the sidewall angle is related to the width of the Gaussian beam shape. However, the difference may be explained by the fact that the authors also modify the dose per pixel when varying the current and the investigated dose and hole diameter differ. Our results suggest, for currents in the studied ion current range between 9.7 and 48 pA, that there is no direct relation between the current (which determines the spot size and shape of the tails of the beam) and the sidewall angle. The main reason for this is that redeposition is the dominant effect.

6. Conclusions

We have shown that it is necessary to deposit a metal (here platinum) before making cross-sections to avoid perturbation of submicrometre milled holes through redeposition, and to achieve a large contrast. The large contrast was needed to determine parameters such as the sidewall angle, milling depth and hole diameter with high precision. Two different routines for scanning the beam over the sample were compared for milling in silicon, SOI and silicon membranes: raster scanning and spiral scanning. The spiral method has the advantage that the amount of structure lowering (sinking of the structure within the substrate) and interhole milling can be reduced significantly. We also found a slight increase in verticality of the sidewall angles and an increase in symmetry of the hole for the spiral scan routine applied to silicon and SOI. The study on the silicon membranes showed that, using the spiral method, it is possible to achieve sidewall angles as small as 1.5°, which is comparable to state of the art dry etching achievements in silicon.

Further optimizations were explored by varying the dose applied to a single hole and to a hole as part of an array, while fixing the dwell time at 0.1 ms. We found that the sidewall angle at half the hole depth can be decreased to values of about 5° in Si. Furthermore, we experimentally showed the non-linear relationship between the depth and dose for submicrometre holes. We found that due to the proximity effects presented here, we obtain a slightly higher milling rate for the holes in an array than for single holes. In the studied dose range we observed also a constant difference between the absolute depth h_{abs} and the relative depth h_{rel}. The impact of the combination dwell time and loop number was investigated by fixing the dose at 69 pC and varying the number of loops between two and 200 and the dwell time between 0.6 ms and 6 μs in Si. The most favourable combination with respect to the hole geometry was found to be a small loop number in combination with a relatively high dwell time of 1 ms. The results seem to contradict with other findings in which smaller dwell times are recommended. Therefore, we assume that the number of loops at a fixed dose per hole is the best optimization

Table 5. Values obtained from milling an array[a] of holes in silicon.

Loop number	Dose per hole[b] D (pC)	Absolute depth, $h_{abs} \pm 3\%$ (nm)	Relative depth, $h_{rel} \pm 3\%$ (nm)	Average diameter, $d_{avg} \pm 10\%$ (nm)	Sidewall angle $\pm 10\%$ (deg)
3	17	83	68	310	53
6	35	160	141	290	20
12	69	320	292	261	11
30	173	872	766	220	8
60	345	1168	1065	222	6
90	518	1312	1224	217	5

[a] Lattice constant 440 nm, hole diameter 250 nm.
[b] Milled at 48 pA using a 0.1 ms dwell time.

Table 6. Effect of dose[a]–loop number variation in an array[b] of holes.

Loops	Dwell time (ms)	Absolute depth, $h_{abs} \pm 3\%$ (nm)	Relative depth, $h_{rel} \pm 3\%$ (nm)	Average diameter, $d_{avg} \pm 5\%$ (nm)	Sidewall angle $\pm 5\%$ (deg)
2	0.6	396	386	252	8.4
6	0.2	355	345	266	10.0
20	0.06	345	335	281	11.8
120	0.001	316	307	287	12.2
200	0.006	314	294	281	13.4

[a] The dose was fixed at 69 pC.
[b] Lattice constant 440 nm, hole diameter 250 nm.

parameter with respect to the sidewall angles (redeposition) and not necessarily only the dwell time. In SOI we found a similar result for the combination of dwell time and loop number for beam currents of 9.7 and 48 pA.

Acknowledgments

This research was supported by NanoNed, a national nanotechnology program coordinated by the Dutch ministry of Economic Affairs, and was also supported by the European Network of Excellence ePIXnet. Laurens Kuipers would like to acknowledge the ‘Stichting voor Fundamenteel Onderzoek der Materie (FOM)’, which is financially supported by the ‘Nederlandse Organisatie voor Wetenschappelijk Onderzoek (NWO)’.

References

[1] Melloni A, Monguzzi P, Costa R and Martinelli M 2003 Design of curved waveguides: the matched bend *J. Opt. Soc. Am.* A **20** 130–37
[2] Villeneuve P R, Fan S and Joannopoulos J 1996 Microcavities in photonic crystals: mode symmetry, tunability, and coupling efficiency *Phys. Rev.* B **54** 7837–42
[3] Chakravarty S, Topol’ancik J, Bhattacharya P, Chakrabarti S, Kang Y and Meyerhoff M E 2005 Ion detection with photonic crystal microcavities *Opt. Lett.* **30** 2578–80
[4] Noda S, Yokoyama M, Imada M, Chutinan A and Mochizuki M 2001 Polarization mode control of two-dimensional photonic crystal laser by unit cell structure design *Science* **293** 1123–5
[5] Akahane Y, Asano T, Song B S and Noda S 2003 High-Q photonic nanocavity in a two-dimensional photonic crystal *Nature* **425** 944–7
[6] Kuramochi E, Notomi M, Mitsugi S, Shinya A, Tanabe T and Watanabe T 2006 Ultrahigh-Q photonic crystal nanocavities realized by the local width modulation of a line defect *Appl. Phys. Lett.* **88** 041112
[7] Notomi M, Shinya A, Mitsugi S, Kira G, Kuramochi E and Tanabe T 2005 Optical bistable switching action of Si high-Q photonic-crystal nanocavities *Opt. Express* **13** 2678–87
[8] Gersen H, Karle T J, Engelen R J P, Bogaerts W, Korterik J P, van Hulst N F, Krauss T F and Kuipers L 2005 Direct observation of Bloch harmonics and negative phase velocity in photonic crystal waveguides *Phys. Rev. Lett.* **94** 123901
[9] Vlasov Y A, O’Boyle M, Hamann H F and McNab S J 2005 Active control of slow light on a chip with photonic crystal waveguides *Nature* **438** 65–9
[10] Johnson S G, Fan S H, Villeneuve P R, Joannopoulos J D and Kolodziejski L A 1999 Guided modes in photonic crystal slabs *Phys. Rev.* B **60** 5751–8
[11] Chou S Y, Krauss P R and Renstrom P J 1996 Nanoimprint lithography *J. Vac. Sci. Technol.* B **14** 4129–33
[12] Hopman W C L, Van Der Werf K O, Hollink A J F, Bogaerts W, Subramaniam V and De Ridder R M 2006 Nano-mechanical tuning and imaging of a photonic crystal micro-cavity resonance *Opt. Express* **14** 8745–52
[13] Bostan C G and de Ridder R M 2002 Design of photonic crystal slab structures with absolute gaps in guided modes *J. Optoelectron. Adv. Mater.* **4** 921–8
[14] Bostan C G, De Ridder R M, Gadgil V J, Kelderman H, Kuipers L and Driessen A 2004 Design and fabrication of line-defect waveguides in hexagon-type SOI photonic crystal slabs: Photonics Europe (Strasbourg) *Proc. SPIE* **5450** 323–32
[15] Fu Y and Bryan N K A 2001 Experimental study of microcylindrical lenses fabricated using focused-ion-beam technology *J. Vac. Sci. Technol.* B **19** 1259–63
[16] Ito T, Ishikawa H, Egawa T, Jimbo T and Umeno M 1997 Fabrication of flat end mirror etched by focused ion beam for GaN-based blue-green laser diode *Japan. J. Appl. Phys.* **36** 7710–1
[17] Chelnokov A, Wang K, Rowson S, Garoche P and Lourtioz J M 2000 Near-infrared Yablonovite-like photonic crystals by focused-ion-beam etching of macroporous silicon *Appl. Phys. Lett.* **77** 2943–5
[18] Lezec H J and Thio T 2004 Diffracted evanescent wave model for enhanced and suppressed optical transmission through subwavelength hole arrays *Opt. Express* **12** 3629–51
[19] Klein Koerkamp K J K, Enoch S, Segerink F B, van Hulst N F and Kuipers L 2004 Strong influence of hole shape on extraordinary transmission through periodic arrays of subwavelength holes *Phys. Rev. Lett.* **92** 183901
[20] Wang K, Filloux P, Paraire N, Roca I and CabarrocasBulkin P 2003 Two-dimensional photonic crystals by focused-ion-beam etching of multilayer membranes *J. Vac. Sci. Technol.* B **21** 966–9
[21] Brezna W, Wanzenböck H, Lugstein A, Bertagnolli E, Gornik E and Smoliner J 2003 Scanning capacitance microscopy investigations of focused ion beam damage in silicon *Physica* E **19** 178–82
[22] Pellerin J G, Shedd G M, Griffis D P and Russell P E 1989 Characterization of focused ion-beam micromachined features *J. Vac. Sci. Technol.* B **7** 1810–2
[23] Kim Y K, Danner A J, Raftery J J and Choquette K D 2005 Focused ion beam nanopatterning for optoelectronic device fabrication *IEEE J. Sel. Top. Quantum Electron.* **11** 1292–8
[24] Knights A P and Hopper G E 2003 Effect of ion implantation induced defects on optical attenuation in silicon waveguides *Electron. Lett.* **39** 1648–9
[25] Cryan M J, Hill M, Sanz D C, Ivanov P S, Heard P J, Tian L, Yu S Y and Rorison J M 2005 Focused ion beam-based fabrication of nanostructured photonic devices *IEEE J. Sel. Top. Quantum Electron.* **11** 1266–77
[26] Schrauwen J, Van Thourhout D and Baets R 2006 Focused-ion-beam fabricated vertical fiber couplers on silicon-on-insulator waveguides *Appl. Phys. Lett.* **89** 141102

[27] Chyr I, Lee B, Chao L C and Steckl A J 1999 Damage generation and removal in the Ga+focused ion beam micrmachining of GaN for photonic applications *J. Vac. Sci. Technol.* B **17** 3063–7
[28] Tanaka Y, Tymczenko M, Asano T and Noda S 2006 Fabrication of two-dimensional photonic crystal slab point-defect cavity employing local three-dimensional structures *Japan. J. Appl. Phys.* 1 **45** 6096–102
[29] Lehrer C, Frey L, Petersen S, Ryssel H, Schafer M and Sulzbach T 2004 Integration of field emitters into scanning probe microscopy sensors using focused ion and electron beams *J. Vac. Sci. Technol.* B **22** 1402–6
[30] Chaix N, Landis S, Hermelin D, Leveder T, Perret C, Delaye V and Gourgon C 2006 Influence of mold depth on capillary bridges in nanoimprint lithography *J. Vac. Sci. Technol.* B **24** 3011–5
[31] Li H W, Kang D J, Blamire M G and Huck W T S 2003 Focused ion beam fabrication of silicon print masters *Nanotechnology* **14** 220–3
[32] Hopman W C L, De Ridder R M, Selvaraja S, Bostan C G, Gadgil V J, Kuipers L and Driessen A 2006 Realization of 2-dimensional air-bridge silicon photonic crystals by focused ion beam, milling and nanopolishing: photonics Europe (Strasbourg) *Proc. SPIE* **6182** 167–73
[33] Tanaka Y, Asano T, Akahane Y, Song B S and Noda S 2003 Theoretical investigation of a two-dimensional photonic crystal slab with truncated cone air holes *Appl. Phys. Lett.* **82** 1661–3
[34] Prenitzer B I, Urbanik-Shannon C A, Giannuzzi L A, Brown S R, Irwin R B, Shofner T L and Stevie F A 2003 The correlation between ion beam/material interactions and practical FIB specimen preparation *Microsc. Microanal.* **9** 216–36
[35] Fu Y, Bryan N K A, Shing O N and Hung N P 2000 Influence of the redeposition effect for focused ion beam 3D micromachining in silicon *Int. J. Adv. Manuf. Technol.* **16** 877–80
[36] Frey L, Lehrer C and Ryssel H 2003 Nanoscale effects in focused ion beam processing *Appl. Phys.* A **76** 1017–23
[37] Lipp S, Frey L, Lehrer C, Frank B, Demm E and Ryssel H 1996 Investigations on the topology of structures milled and etched by focused ion beams *J. Vac. Sci. Technol.* B **14** 3996–9
[38] Balasubramanian K, Heard P J and Cryan M J 2006 Focused ion beam fabrication of two dimensional photonic crystals in silicon-on-insulator *J. Vac. Sci. Technol.* B **24** 2533–7
[39] Yamaguchi H, Shimase A, Haraichi S and Miyauchi T 1984 Characteristics of silicon removal by fine focused gallium ion beam *J. Vac. Sci. Technol.* B **3** 71–4
[40] Fu Y, Bryan N K A, Shing O N and Wyan H N P 2000 Influence analysis of dwell time on focused ion beam micromachining in silicon *Sensors Actuators* A **79** 230–4
[41] Adams D P and Vasile M J 2006 Accurate focused ion beam sculpting of silicon using a variable pixel dwell time approach *J. Vac. Sci. Technol.* B **24** 836–44
[42] Nellen P M, Callegari V and Brönnimann R 2006 FIB-milling of photonic structures and sputtering simulation *Microelectron. Eng.* **83** 1805–8
[43] Tseng A A 2004 Recent developments in micromilling using focused ion beam technology *J. Micromech. Microeng.* **14** R15–34
[44] Lugstein A, Basnar B, Smoliner J and Bertagnolli E 2003 FIB processing of silicon in the nanoscale regime *Appl. Phys.* A **76** 545–8
[45] Bischoff L, Teichert J and Heera V 2001 Focused ion beam sputtering investigations on SiC *Appl. Surf. Sci.* **184** 372–6
[46] McNab S J, Moll N and Vlasov Y A 2003 Ultra-low loss photonic integrated circuit with membrane-type photonic crystal waveguides *Opt. Express* **11** 2927–39
[47] Settle M, Salib M, Michaeli A and Krauss T F 2006 Low loss silicon on insulator photonic crystal waveguides made by 193 nm optical lithography *Opt. Express* **14** 2440–5
[48] Lehrer C, Frey L, Petersen S and Ryssel H 2001 Limitations of focused ion beam nanomachining *J. Vac. Sci. Technol.* B **19** 2533–8
[49] Wilhelmi O, Reyntjens S, Wall D, Geurts R, Jiao C and Roussel L 2006 *Nanofabrication and Rapid Prototyping with DualBeam Instruments: Conf. Micro- and Nano-Engineering (Barcelona)*